



DOI: [10.29026/oes.2022.210008](https://doi.org/10.29026/oes.2022.210008)

Photonic lenses with whispering gallery waves at Janus particles

Igor V. Minin¹, Oleg V. Minin¹, Yinghui Cao², Bing Yan³, Zengbo Wang³
and Boris Luk'yanchuk^{4*}

We show that electric field on the plane surface of truncated sphere or cylinders (so called Janus particles) have sharp resonances versus the depth of removed segment of a sphere or cylinder. These resonances are related to the excited whispering gallery waves caused by truncation. It is a new mechanism of the field localization. Optimization of this effect for cylinders permits to reach a super resolution in the line thickness, which can be used for contact optical lithography.

Keywords: photonics; whispering gallery mode; whispering gallery waves; Janus particles

Minin IV, Minin OV, Cao YH, Yan B, Wang ZB et al. Photonic lenses with whispering gallery waves at Janus particles. *Opto-Electron Sci* 1, 210008 (2022).

Introduction

Development of optical lithography with nanoscale resolution has been a long-standing goal for the nanotechnology community¹. Among the many suggested methods there were a lithography with transparent dielectric particles which were used as a microscopic lenses^{2–5}. The basic physical features of this technique can be well understood from the Mie theory⁶ and also from the more complicated problem “particle on surface”^{7,8}. According to these calculations, a transparent dielectric sphere with a diameter of more than three wavelengths of radiation incident on it can function either as a focusing lens (photon jet mode) or as a resonator concentrating energy in the whispering gallery waves in the wall region⁹. A similar behavior is shown by a transparent cylinder. The transition from the photon jet mode to the resonator mode with whispering gallery waves occurs when the size of the sphere or the radiation wavelength changes. Both phenomena are perfectly described in the frame-

work of Mie theory, see e.g.¹⁰. New phenomena arise in particles in which a segment of a sphere or cylinder is removed (Janus particles^{11,12}). It is a typical design of solid immersion lens^{13,14}. It is known that parameters of a photonic jet from a hemisphere (or hemicylinder) can be very different from the parameters of a jet formed by a whole sphere¹⁵ or cylinder¹⁶.

In the present paper we show that parameter of whispering gallery waves can be also quite different from the whole sphere or cylinder. Optimization of the remote segment thickness permits to create highly localized field distribution. This effect in cylinders can be used for contacting optical lithography with super resolution in the line thickness.

Photonic nanojet: from geometrical optics approximation to the Mie theory

A spherical transparent particle can focus light. This ef-

¹Tomsk Polytechnic University, 36 Lenin Avenue, Tomsk 634050, Russia; ²College of Computer Science and Technology, Jilin University, 2699 Qianjin Street, Changchun 130012, China; ³School of Computer Science and Electronic Engineering, Bangor University, Dean Street, Bangor, Gwynedd, LL57 1UT, UK; ⁴Faculty of Physics, Lomonosov Moscow State University, Moscow 119991, Russia.

*Correspondence: B Luk'yanchuk, E-mail: lukiyanichuk@nanolab.phys.msu.ru

Received: 14 September 2021; Accepted: 18 December 2021; Published online: 16 February 2022



Open Access This article is licensed under a Creative Commons Attribution 4.0 International License.

To view a copy of this license, visit <http://creativecommons.org/licenses/by/4.0/>.

© The Author(s) 2022. Published by Institute of Optics and Electronics, Chinese Academy of Sciences.

fect has been known for a few millennia: for example, Pliny the Elder (AD 23–AD 79) reported on the incendiary action of glass spheres⁹. This effect is easy to understand under geometric optics approximation^{17,18}. The simplest way is to use ray tracing¹⁹ and Snell's law^{20,21} (this technique has been known since Kepler). Refracted rays form a caustic, which is presented by parametric equation (here all coordinates x and y are normalized by particle radius, R):

$$\begin{aligned} x_c &= \left[1 - \frac{1}{2} \frac{\sqrt{n^2 - 1 + \cos^2 \varphi} - 2 \cos \varphi}{\sqrt{n^2 - 1 + \cos^2 \varphi} - \cos \varphi} \cos \varphi \right] \cos \psi, \\ y_c &= \sec \psi \sin \varphi + x_c \tan \psi, \end{aligned} \quad (1)$$

where $\psi = 2 \left[\varphi - \arcsin \left(\frac{\sin \varphi}{n} \right) \right]$.

Such caustic is presented by cuspid curve^{22,23}, as in Fig. 1. The singularity point (geometrical optics focus²⁴) is situated at

$$x_s = x_c|_{\varphi \rightarrow 0} = \frac{n}{2(n-1)}. \quad (2)$$

Thus, $x_s \rightarrow \infty$ at $n \rightarrow 1$ and $x_s \rightarrow 1$ at $n \rightarrow 2$. When $n > 2$ the caustic is situated inside the sphere, this is the case of materials with a high refractive index. Such materials are used in optically resonant dielectric nanostructures²⁵, while materials with a refractive index of less than two⁹ are the main materials for most optical components (lenses, optical fibers, etc.). This caustic was analyzed in a number of papers due to the problem of photonic nanojet, see ref.⁹ and references there. From the Eq. (1) one should define the numerical aperture $NA = n \sin \chi$, where the angle χ calculated at the surface of the particle, i.e., at $\varphi = \arccos \sqrt{\frac{n^2 - 1}{3}}$. This estima-

tion yields $NA = n \sqrt{\frac{4 - n^2}{3}}$. Maximal field enhancement in the focal point can be estimated as $I = [\sin \varphi_a / y_c(\varphi_a)]^2$, where $\varphi_a = \arccos \sqrt{(n^2 - 1)/3}$. Position of geometrical optics focus can be approximated by

$$x_f = \frac{2n^6 + 9n^4 + 48n^2 - 32}{6n^2(2 + n^2)\sqrt{3(n^2 - 1)}}. \quad (3)$$

The solution with ray tracing yields just a qualitative picture of light focusing. One can compare this solution with the exact solution which follows from the Mie theory⁶. However, the approximation of geometrical optics is valid just for sufficiently big size parameter $q = 2\pi R/\lambda \gg 1$ (here R is radius of the particle and λ is radiation wavelength). Thus, exact solution requires the summation of a large number of terms, $\ell_{\max} = q + 4.05 q^{1/3} + 2$ ²⁶, in a multipole expansion even for moderate sphere sizes. For such big particles one can use the method of uniform caustic asymptotic¹⁸. The lowest nontrivial order correction for the field distribution is related to Bessoid integral. This integral appears naturally in the paraxial approximation²⁴. Results of calculations are shown in Fig. 2.

According to the Mie theory^{6,26} the scattering efficiency $Q_{\text{sca}} = \sigma_{\text{sca}}/(\pi R^2)$ (here σ_{sca} is scattering cross section) can be expressed as a sum of electric $Q_\ell^{(e)}$ and magnetic $Q_\ell^{(m)}$ scattering efficiencies associated with the multipolar moment of ℓ the order multipoles:

$$\begin{aligned} Q_{\text{sca}} &= \sum_{\ell=1}^{\infty} (Q_\ell^{(e)} + Q_\ell^{(m)}), \quad Q_\ell^{(e)} = \frac{2}{q_m^2} (2\ell + 1) |a_\ell|^2, \\ Q_\ell^{(m)} &= \frac{2}{q_m^2} (2\ell + 1) |b_\ell|^2, \end{aligned} \quad (4)$$

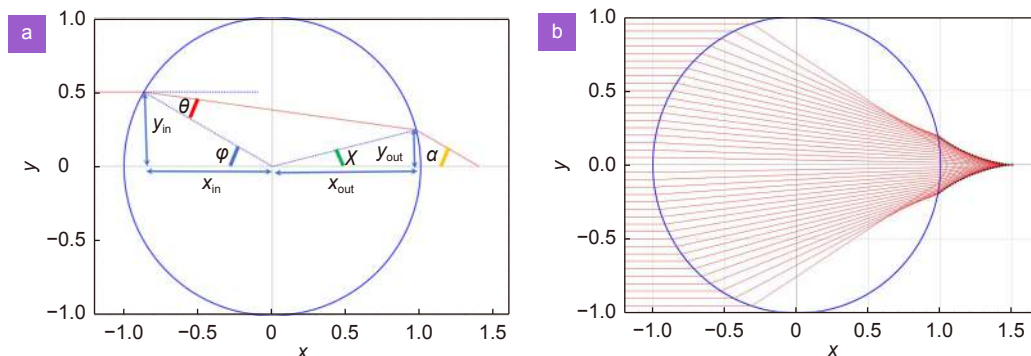


Fig. 1 | (a) Ray tracing for a big particle with radius $R \gg \lambda$. We introduce the incidence angle φ and the refraction angle θ inside the sphere $\sin \varphi = n \sin \theta$. The ray enter into the particle at the point with coordinates $y_{\text{in}} = \tan \varphi$ and $x_{\text{in}} = -\cos \varphi$. The angles χ and α are given by $\chi = 2\theta - \varphi$ and $\alpha = 2\varphi - 2\theta$. Two close rays y_c and y_{cc} (corresponding to angles φ and $\varphi + \delta\varphi$) emerged from the sphere after the second refraction are crossing at the caustic point $x_c = x_{\text{out}} + \partial_\varphi \sin \chi / \partial_\varphi \tan \alpha$. This yields the Eq. (1) for caustic. (b) The shape of the caustic from the Eq. (1) for the sphere with $n = 1.5$ is shown by dashed black line.

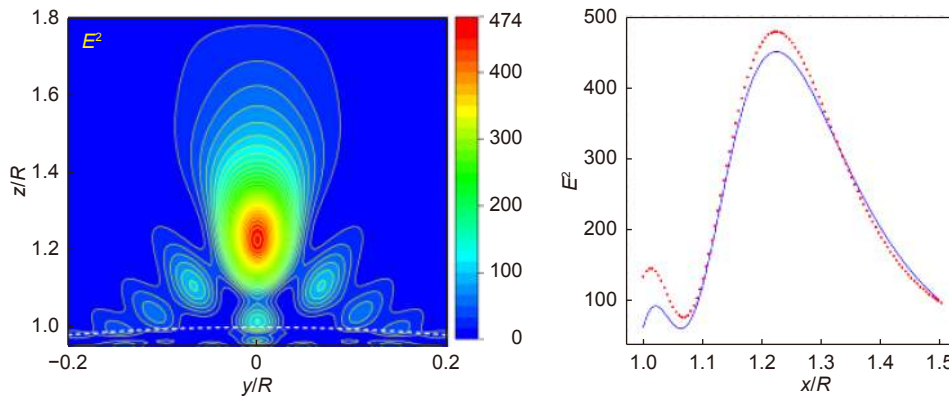


Fig. 2 | (a) Distribution of intensity calculated from the Mie theory with $n = 1.5$ and $q = 70$. Such distribution is typical for Bessoid matching solution, see e.g., Fig. 5 in ref.²⁴. (b) Intensity distribution according to Bessoid approximation²⁴ (solid blue line) and from the Mie theory (dotted red line).

where the electric a_ℓ and magnetic b_ℓ scattering amplitudes are defined by formulas

$$a_\ell = \frac{\Re_\ell^{(a)}}{\Re_\ell^{(a)} + i\Im_\ell^{(a)}}, \quad b_\ell = \frac{\Re_\ell^{(b)}}{\Re_\ell^{(b)} + i\Im_\ell^{(b)}}, \quad (5)$$

with $\Re_\ell^{(a,b)}$ and $\Im_\ell^{(a,b)}$ coefficients expressed by

$$\begin{aligned} \Re_\ell^{(a)} &= n_p \psi_\ell(q_p) \psi'_\ell(q_m) - n_m \psi_\ell(q_m) \psi'_\ell(q_p), \\ \Im_\ell^{(a)} &= n_p \psi_\ell(q_p) \chi'_\ell(q_m) - n_m \chi_\ell(q_m) \psi'_\ell(q_p), \\ \Re_\ell^{(b)} &= n_p \psi_\ell(q_m) \psi'_\ell(q_p) - n_m \psi_\ell(q_p) \psi'_\ell(q_m), \\ \Im_\ell^{(b)} &= n_p \chi_\ell(q_m) \psi'_\ell(q_p) - n_m \chi'_\ell(q_m) \psi_\ell(q_p). \end{aligned} \quad (6)$$

Here the functions $\psi_\ell(z) = \sqrt{\frac{\pi z}{2}} J_{\ell+\frac{1}{2}}(z)$ and $\chi_\ell(z) = \sqrt{\frac{\pi z}{2}} N_{\ell+\frac{1}{2}}(z)$ are expressed through the Bessel and Neumann functions¹⁰. We use the subscripts m and p to denote the values referring to the external media and the particle, with refractive indices n_m and n_p , respectively. In the expressions above, $q_m = q n_m$ and $q_p = q n_p$. The symbol q represents the so-called size parameter, defined as $q = \omega R / c = 2\pi R / \lambda$.

The electric and magnetic fields inside the particle are expressed through the internal scattering amplitudes c_ℓ and d_ℓ given by⁶

$$c_\ell = \frac{in_p}{\Re_\ell^{(a)} + i\Im_\ell^{(a)}}, \quad d_\ell = \frac{in_p}{\Re_\ell^{(b)} + i\Im_\ell^{(b)}}. \quad (7)$$

Although the denominators of these amplitudes are the same as in amplitudes a_ℓ and b_ℓ in Eq. (5), which means that position of these resonances are close, the numerators of Eq. (7) never tends to zero. As a result the values of amplitudes $|c_\ell|^2$ and $|d_\ell|^2$ are not restricted by unity as amplitudes $|a_\ell|^2$ and $|b_\ell|^2$ in Eq. (5), but increase with values of size parameter and refractive index. To compare amplitudes it is convenient to introduce partial

internal scattering efficiencies, similar to those in Eq. (4):

$$F_\ell^{(e)} = \frac{2}{q_m^2} (2\ell + 1) |c_\ell|^2, \quad F_\ell^{(m)} = \frac{2}{q_m^2} (2\ell + 1) |d_\ell|^2. \quad (8)$$

It leads to specific variation of c_ℓ and d_ℓ amplitudes at the big ℓ values. Namely, the amplitudes of these functions are quite small up to some threshold values, $q < q_{tr}$, which are of the order of $\ell^{10,27}$, see an example in Fig. 3. The first narrow resonance at $q = q_{tr}$, where $q_{tr} \cong \ell$, plays a dominant role in the Mie theory. The total electric field E (similar in H) can be presented as a sum of a single resonant term $E_{\ell=\ell_{res}}$ with a narrow spectrum and the field from all other nonresonant terms $\sum_{\ell \neq \ell_{res}} E_\ell$ with a broad spectrum. The interference of the signals with a broad and narrow spectums yields the Fano resonance, which produces the narrow resonances in the intensity. These resonances in electric and magnetic fields greatly exceed corresponding resonances in the scattering efficiency¹⁰.

The electric and magnetic fields can be defined

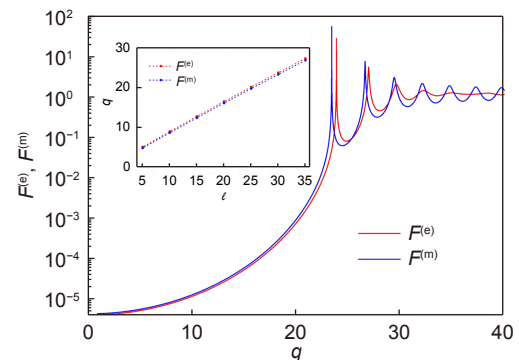


Fig. 3 | Amplitudes $|F_\ell^{(e)}|$ and $|F_\ell^{(m)}|$ for $\ell = 30$ and $n_p = 1.5$ versus size parameter q . The first sharp resonance arise at q by the order of ℓ . Insert shows how the position of the first sharp resonance vary with ℓ number.

through the derivations of the electric, $\Pi^{(e)} = \sum \Pi_\ell^{(e)}$, and magnetic, $\Pi^{(m)} = \sum \Pi_\ell^{(m)}$, Debye potentials¹⁷. Inside the particle these potentials are presented by¹⁷

$$\begin{aligned}\Pi_\ell^{(e)} &= c_\ell \frac{i^{\ell+1}}{k^2} \frac{2\ell+1}{\ell(\ell+1)} \psi_\ell(kr) P_\ell^{(1)}(\cos\theta) \cos\varphi, \\ \Pi_\ell^{(m)} &= d_\ell \frac{i^{\ell+1}}{k^2} \frac{2\ell+1}{\ell(\ell+1)} \psi_\ell(kr) P_\ell^{(1)}(\cos\theta) \sin\varphi.\end{aligned}\quad (9)$$

Here k is the wave vector inside the particle, $kR = q_p$.

From the Eq. (9) one explains the physical origin of the whispering gallery waves (WGW) formation²⁸. Argument spherical Bessel function $\psi_\ell(kr)$ varies from zero in the center of the particle till parameter q_p on the surface of the particle. Thus, at big ℓ values ψ_ℓ function is close to zero till to critical value q_p which is by the order of ℓ , see in Fig. 4(a). If the first zero of the Bessel function is located near the radius of the sphere, then almost the entire field of this wave will be located in a very narrow region near the surface of the sphere. This is the WGW case. The angular field modulation is presented by Legendre function, see in Fig. 4(b).

The WGW can be interpreted as a wave of total internal reflection of the ray propagating along the surface of the dielectric sphere²⁸. However, if the interface has a curvature (as in the case of the sphere), then the internal reflection is not complete: part of the wave still seeps out of the ball out. One can see this leakage in Fig. 4(b). It occurs through the white triangles situated on the surface of the particle. The leakage is the smaller, the larger the radius of the ball in comparison with the wavelength. That is, for the existence of WGW, the sphere must have a rather sick radius in comparison with the wavelength of light, i.e., it needs the condition $q_p \gg 1$. Calculations with the Mie theory show that the WGW structure in the

electric field intensity can be seen even at the size parameter by the order of ten, see in Fig. 5.

Janus particle: from geometrical optics to the whispering gallery waves.

One can examine the light focusing by truncated cylinder or a sphere, see in Fig. 6. Truncated segment can be replaced by a similar portion of different material – such structures are called as Janus particles²⁹. We use notation h for the height of truncated segment. In particular case replaced portion can be an air or vacuum. In simulations (here and below) the models were built by using a finite integral technique (FIT) realized in commercial software package - CST Microwave Studio. Tetrahedral meshes and triangular grids were fitted with ‘open space’ boundary condition along all directions (x, y, z) to approach better accuracy for simulation. Mesh sizes were set to $\lambda/15$ for particle and $\lambda/10$ for background. The ray tracing technique applied for truncated sphere yields the following shape of the caustics:

$$\begin{aligned}z_c &= 1 - h - \frac{\sec\beta}{n} \frac{(1 - n^2 \sin^2\beta)^{3/2}}{\cos\varphi - \sqrt{n^2 - \sin^2\varphi}} \\ &\cdot \left[\cos\varphi \sqrt{n^2 - \sin^2\varphi} + (1 - h + \cos\varphi) \sec^2\beta \right. \\ &\cdot \left. \left(\cos\varphi - \sqrt{n^2 - \sin^2\varphi} \right) + \sin\varphi \sqrt{n^2 - \sin^2\varphi} \tan\beta \right],\end{aligned}\quad (10)$$

$$\begin{aligned}y_c &= y_{\text{out}} - (z_c - 1 + h) \tan\gamma, \\ y_{\text{out}} &= \sin\varphi - (1 - h + \cos\varphi) \tan(\varphi - \theta), \\ \gamma &= \arcsin[n \sin(\varphi - \theta)], \\ \beta &= \varphi - \theta, \quad \theta = \arcsin\left(\frac{\sin\varphi}{n}\right).\end{aligned}\quad (11)$$

The singularity point this Janus particle situated at

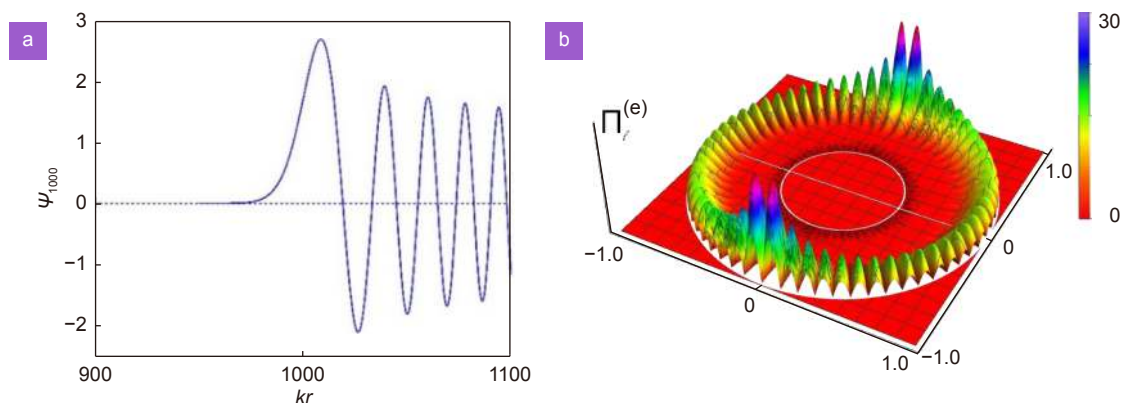


Fig. 4 | (a) Spherical Bessel function $\psi_\ell(kr)$ at big index $\ell = 1000$ ²⁸. (b) Spatial distribution of the modulus of the $\Pi_\ell^{(e)}$ function (9) at $\varphi = 0$ and $\ell = 30$ for $n = 1.5$ and $q = 23.855$.

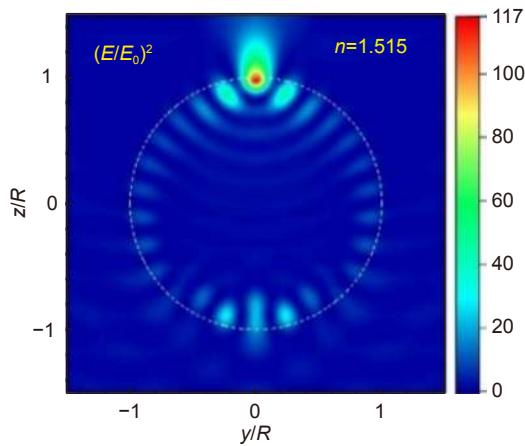


Fig. 5 | Distribution of electric intensity $(E/E_0)^2$ within the yz plane of the particle with refractive index $n = 1.515$ and size parameter $q = 11$.

$$z_f = z_c|_{\varphi \rightarrow 0} = 1 - \frac{2}{n} + \frac{1}{n-1} + h \left(\frac{1}{n} - 1 \right). \quad (12)$$

The basic effect with Janus particle is related to variation of focal length in comparison with the initial sphere. For example, the sphere with $n = 1.33$ has the focal point situated at $z_f = 2.015$. After small truncation with $h = 0.07$ corresponding Janus particle has a focal point with $z_f = 2.509$, i.e., truncation yields the longer focus. The ray tracing technique¹⁹ approximation gave qualitatively correct description of focusing properties of transparent dielectric.

The truncated particle presents a solid immersion lens (SIL) which can overcome diffraction limit¹³. It could be noted that physical principles of truncated spherical SIL, for which aberration free focusing occurs and also known as Weierstrass SIL, is based on compressing the emitted light into a small NA by decreasing of the refraction angle of the transmitted light, measured from the optical axis. This occurs when the sphere is truncated to a thickness $h = r(1 + 1/n)$, where r is the radius of the

sphere, and h corresponds to the aplanatic focus, see in ref.¹⁷ (page 253) and ref.³⁰. Similar SIL have been used in optical microscopes and photolithography³¹. Analysis of the photonic nanojet with truncated spherical particle shows that the maximal intensity in the focal point is less than those produced by spherical particle, but the effective focal length can be much greater¹⁵.

We repeated a similar numerical analysis for a different design of Janus particles and found some new effects. As an example, we show in Fig. 7 the cylindrical Janus particle consisting from two half cylinders with different refractive index: $n = 1.5$ for the bottom part and $n = 1.3$ for the upper part. The diameter of a whole cylinder is equal to $2R = 5\lambda$. Thus, the size parameter $q = 5\pi \gg 1$. At normal condition one can see a usual photon nanojet with maximal field enhancement $E^2 = 17$ at the focal point. A small truncation with $h = d/R = 0.03$ leads to the field redistribution due to strong WGW excitation with maximal field enhancement $E^2 = 23.5$. A further truncation with $h = 0.04$ practically restore the initial photon nanojet. A similar behavior can be seen for magnetic intensity variation.

An example of truncation effect for the intensity distribution is shown in Fig. 8. Namely, for the cylinder with refractive index $n = 1.5$ and big size parameter $q = 2\pi R/\lambda = 100$ we can see a number of oscillations with maximal intensity around the particle. These oscillations depend on light polarization and the depth of truncated layer. Amplitudes of these resonances are typically about 10% of average intensity with field enhancement about 25. However, for some small truncation with $d = 0.015R$ we can see in Fig. 8 resonance for TM polarized light with field enhancement in the hot spots on the surface. It looks like resonant excitation of surface electromagnetic wave within the plane disk of the truncated

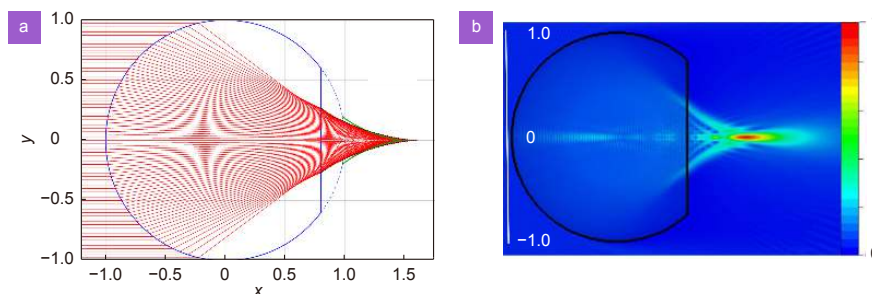


Fig. 6 | (a) We introduce the same incidence angle φ and the refraction angle θ as in Fig. 1(a). Here h is the height of truncation normalized to particle radius R . Ray emerges from the sphere after the second refraction with the angle γ follows the Snell's law $\sin \gamma = n \sin(\varphi - \theta)$. The shape of the caustic for the truncated sphere with $h = 1 - 1/n$ and $n = 1.5$ is shown by dashed black line. The solid green line shows the caustic of the spherical particle with the same refractive index. **(b)** The same parameters and the exact solution of the Maxwell equation, corresponding to size parameter $q = 2\pi R/\lambda = 100$.

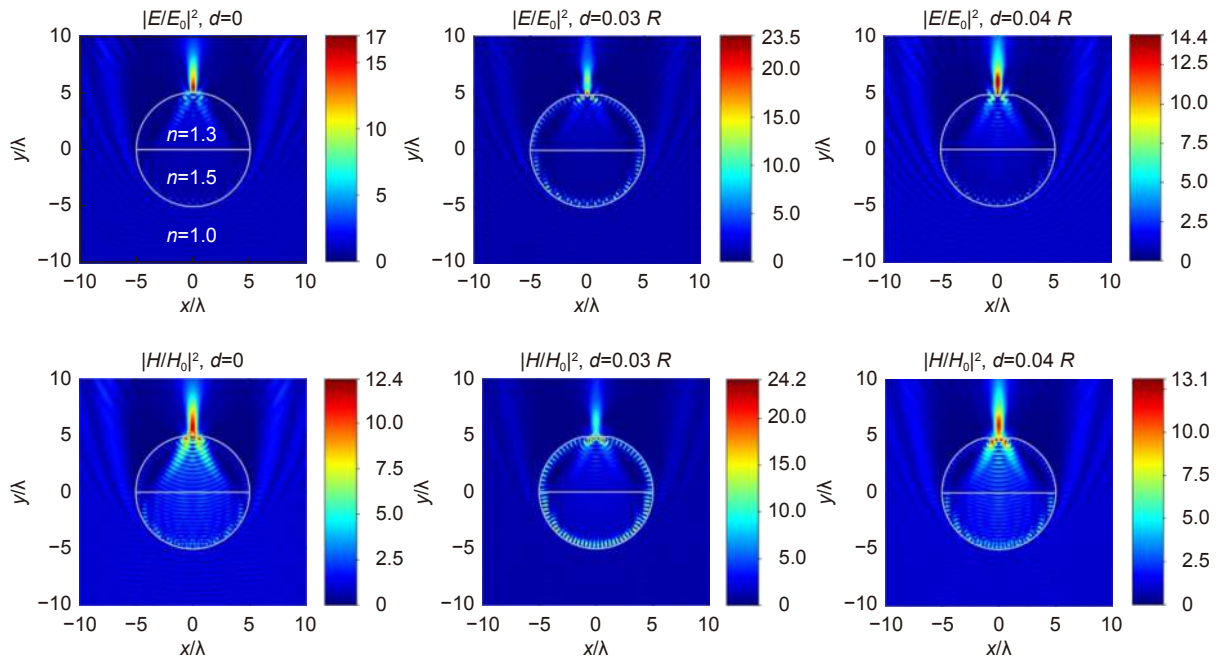


Fig. 7 | Distribution of electric E^2 intensity (pictures on the top) and magnetic H^2 intensity (down pictures) within the cross section of the Janus cylinder with refractive index $n = 1.5$ (down), $n = 1.3$ (top), and size parameter $q = 5\pi$.

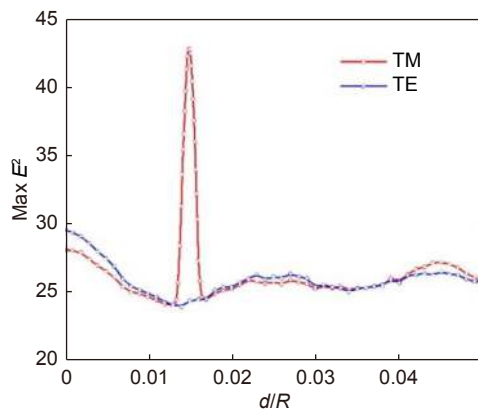


Fig. 8 | Maximal field enhancement around the truncated cylindrical versus the depth of truncated element.

surface. The singularity related to phase discontinuity at the line where the spherical (or cylindrical) surface cross the plane surface leads to change of the Snell's law to generalized laws of reflection and refraction³². Accord-

ing to this law occurs the variation of critical angles for total internal reflection. At some value of phase gradient there is a critical angle of incidence above which the reflected beam becomes evanescent³². Under the approximation of geometrical optics this phase gradient depends on the thickness h of truncated element and refractive index n . In Fig. 9(c) one can see the result of interference of two evanescent waves. We also found that the efficiency of the excitation of whispering gallery waves strongly depends on the h value.

Optimization of this effect for cylinders permits to reach a super resolution in the line thickness which can be used for contacting optical lithography

Truncated nanowires for near field optical lithography

The most powerful modern lithographic technique is related to usage of focused electron beams³³ or ion beams³⁴

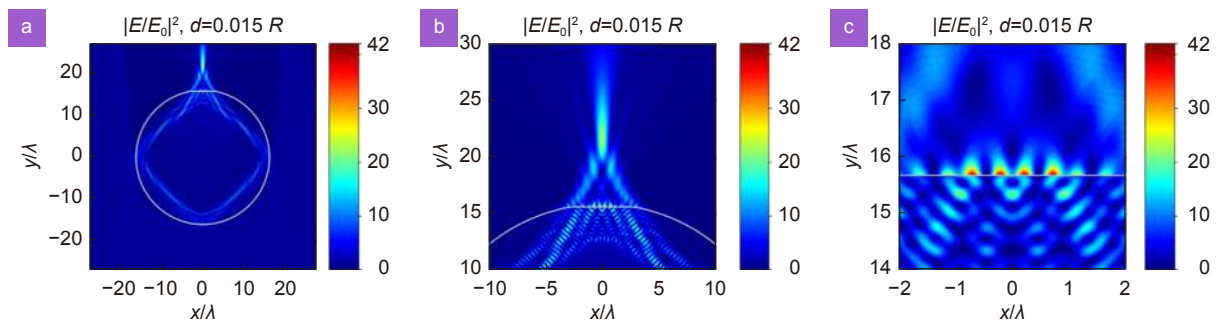


Fig. 9 | Distribution of the field intensity for a resonant value of truncation (a) and zoom in (b) and further (c).

(e.g. a focused helium ion beam³⁵). These techniques permit to realize patterning fidelity at nanometer scale dimensions. However, beam technology is associated with very expensive and complex equipment. In addition, it is rather slow.

Over the past decades, a number of new ideas have been proposed to create a fast-lithographic technique that allows mass production of structures with a scale of tens of nanometers. Among these ideas, for example, an evanescent interferometric lithography^{36–38} can be mentioned. Other techniques involve laser induced tip-assisted Atomic Force Microscope (AFM)³⁹ or a Near-field Scanning Optical Microscope (NSOM)^{40,41}. Finally, we should mention ‘plasmon printing’ technology^{42–44}. The later relies on the surface plasmon resonance occurring in metal nanoparticles, which can produce sub-wavelength structures.

Returning to lithography using Janus particles, we note once again the resonance properties of small truncation of the cylinder, see in Fig. 10. Here we show the maximal intensities inside and outside particle. Each resonance corresponds to resonant excitation of whispering gallery waves. Similar resonances existing within the nontruncated particles as well (see e.g., movie in supplementary materials in ref.⁹). The difference is that in truncated particles these resonances are sharper. We also draw attention to the fact that in Janus particles the magnetic nanojet mode appears to be more contrasting compared to nontruncated particles⁹. It gave the additional functionality to work with magnetic materials.

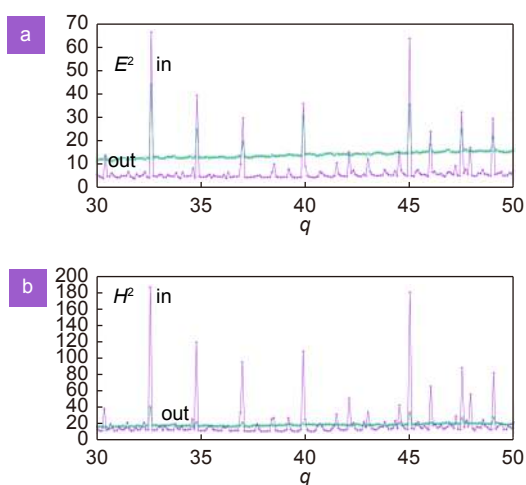


Fig. 10 | Internal and external electric (a) and magnetic (b) intensities versus size parameter for the cylinder with fixed truncation parameter $h = 0.02$. Size parameter $q = 32.5$ corresponds to radius of the cylinder $2R \approx 10\lambda$.

Depending on truncation parameter h and radiation wavelength, one can realize situation with a single, double, or quadruple-maximums distributions in the intensity on the plane truncated surface. Having the spacing between cylinders as additional parameter we can imagine lithographic technique schematically presented in Fig. 11. The number of cylinders with refracted index n_p are embedded into matrix with refracted index $n_m < n_p$. It is equivalent to situation when the cylinders with relative index $n = n_p/n_m$ are situated in vacuum. The surface of this matrix can be polished to reach a precise truncation.

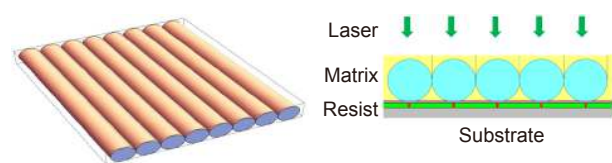


Fig. 11 | Schematic for a lithographic process with truncated cylinders. Here a thin protected layer between the matrix and photoresist plays an important role of anti-reflective coating, depending on the thickness of the coating.

We performed a modeling of this technique to analyze the patterning fidelity at nanometer scale dimensions. The length of the lines can be on a scale of centimeters.

Conclusions

A spherical resonator cannot have an infinite quality factor (Q-factor⁴⁵) due to the violation of the total internal reflection on a curved surface. Recently, many efforts have been made to increase the Q-factor of spherical and dielectric resonators using bound states in continuum^{46,47}. Our research shows that the use of Janus particles also contributes to an increase in the figure of merit and an increase in the electric and magnetic intensity components near the surface of the distant element of the particle. The effect is resonant in relation to the volume of the removed fraction of the substance and is observed in the size range $R: 5\lambda \sim 15\lambda$. The removal of a surface feature in a Janus particle plays a role similar to that of a diamond cut. The smallest cut diamonds are on the order of one millimeter, while the discussed Janus particles are a thousand times smaller.

References

1. Ito T, Okazaki S. Pushing the limits of lithography. *Nature* **406**, 1027–1031 (2000).
2. Lu YF, Zhang L, Song WD, Zheng YW, Luk'yanchuk BS. Laser

- writing of a subwavelength structure on silicon (100) surfaces with particle-enhanced optical irradiation. *J Exp Theor Phys Lett* **72**, 457–459 (2000).
3. Mosbacher M, Münzer HJ, Zimmermann J, Solis J, Boneberg J et al. Optical field enhancement effects in laser-assisted particle removal. *Appl Phys A* **72**, 41–44 (2001).
 4. Münzer HJ, Mosbacher M, Bertsch M, Zimmermann J, Leiderer P et al. Local field enhancement effects for nanostructuring of surfaces. *J Microsc* **202**, 129–135 (2001).
 5. Piglmayer K, Denk R, Bäuerle D. Laser-induced surface patterning by means of microspheres. *Appl Phys Lett* **80**, 4693–4695 (2002).
 6. Bohren CF, Huffman DR. *Absorption and Scattering of Light by Small Particles* (Wiley, New York, 1998).
 7. Bobbert PA, Vlieger J. Light scattering by a sphere on a substrate. *Phys A:Stat Mech Appl* **137**, 209–242 (1986).
 8. Luk'yanchuk BS, Zheng YW, Lu YF. Laser cleaning of solid surface: optical resonance and near-field effects. *Proc SPIE* **4065**, 576–587 (2000).
 9. Luk'yanchuk BS, Paniagua-Domínguez R, Minin IV, Minin OV, Wang ZB. Refractive index less than two: photonic nanojets yesterday, today and tomorrow [Invited]. *Opt Mater Express* **7**, 1820–1847 (2017).
 10. Wang ZB, Luk'yanchuk B, Yue LY, Yan B, Monks J et al. High order Fano resonances and giant magnetic fields in dielectric microspheres. *Sci Rep* **9**, 20293 (2019).
 11. Walther A, Müller AHE. Janus particles. *Soft Matter* **4**, 663–668 (2008).
 12. Hu J, Zhou SX, Sun YY, Fang XS, Wu LM. Fabrication, properties and applications of Janus particles. *Chem Soc Rev* **41**, 4356–4378 (2012).
 13. Mason DR, Jouravlev MV, Kim KS. Enhanced resolution beyond the Abbe diffraction limit with wavelength-scale solid immersion lenses. *Opt Lett* **35**, 2007–2009 (2010).
 14. Lee GJ, Kim HM, Song YM. Design and fabrication of microscale, thin-film silicon solid immersion lenses for mid-infrared application. *Micromachines* **11**, 250 (2020).
 15. Mahariq I, Giden IH, Kurt H, Minin OV, Minin IV. Strong electromagnetic field localization near the surface of hemicylindrical particles. *Opt Quantum Electron* **50**, 423 (2018).
 16. Gu GQ, Shen XL, Peng Z, Yang XF, Bandyopadhyay S et al. Numerical investigation of photonic nanojets generated from D-shaped dielectric microfibers. *Proc SPIE* **11186**, 111861H (2019).
 17. Born M, Wolf E. *Principles of Optics: Electromagnetic Theory of Propagation, Interference and Diffraction of Light* (Cambridge University Press, 7th edition, 1999).
 18. Kravtsov YA, Orlov YI. *Caustics, Catastrophes and Wave Fields* (Springer, Berlin, 1993).
 19. Glassner AS. *An Introduction to Ray Tracing* (London: Academic Press, 1991).
 20. Luk'yanchuk BS, Arnold N, Huang SM, Wang ZB, Hong MH. Three-dimensional effects in dry laser cleaning. *Appl Phys A* **77**, 209–215 (2003).
 21. Arnold N. Theoretical description of dry laser cleaning. *Appl Surf Sci* **208–209**, 15–22 (2003).
 22. Arnold VI. *Catastrophe Theory* Wassermann GS, Thomas RK, trans (Springer Science & Business Media, Berlin, 2003).
 23. Poston T, Stewart I. *Catastrophe Theory and Its Applications* (Courier Corporation, 2014). [https://abigsocialbookmarking.com](https://abigsocialbookmarking.com/search/catastrophe-theory-and-its-applications)
 24. Kofler J, Arnold N. Axially symmetric focusing as a cuspid diffraction catastrophe: scalar and vector cases and comparison with the theory of Mie. *Phys Rev B* **73**, 235401 (2006).
 25. Kuznetsov AI, Miroshnichenko AE, Brongersma ML, Kivshar YS, Luk'yanchuk B. Optically resonant dielectric nanostructures. *Science* **354**, aag2472 (2016).
 26. Barber PW, Hill SC. *Light Scattering by Particles: Computational Methods* (World Scientific, Singapore, 1990).
 27. Yue LY, Wang ZB, Yan B, Monks JN, Joya Y et al. Super-enhancement focusing of Teflon sphere. *Ann Phys* **532**, 2000373 (2020).
 28. Oraevsky AN. Whispering-gallery waves. *Quantum Electron* **32**, 377–400 (2002).
 29. Liu PW, Liu AT, Kozawa D, Dong JY, Yang JF et al. Autoperforation of 2D materials for generating two-terminal memristive Janus particles. *Nat Mater* **17**, 1005–1012 (2018).
 30. Kino GS, Mansfield SM. Near field and solid immersion optical microscope. US Patent 5004307 (1991). <https://www.freepatentsonline.com/5004307.html>
 31. Ghislain LP, Elings VB, Crozier KB, Manalis SR, Minne SC et al. Near-field photolithography with a solid immersion lens. *Appl Phys Lett* **74**, 501–503 (1999).
 32. Yu NF, Genevet P, Kats MA, Aieta F, Tetienne JP et al. Light propagation with phase discontinuities: generalized laws of reflection and refraction. *Science* **334**, 333–337 (2011).
 33. Chen YF. Nanofabrication by electron beam lithography and its applications: a review. *Microelectron Eng* **135**, 57–72 (2015).
 34. Watt F, Bettiol AA, van Kan JA, Teo EJ, Breese MBH. Ion beam lithography and nanofabrication: a review. *Int J Nanosci* **4**, 269–286 (2005).
 35. Kuznetsov AI, Miroshnichenko AE, Fu YH, Viswanathan V, Rahmani M et al. Split-ball resonator as a three-dimensional analogue of planar split-rings. *Nat Commun* **5**, 3104 (2014).
 36. Lim CS, Hong MH, Lin Y, Xie Q, Luk'yanchuk BS et al. Microlens array fabrication by laser interference lithography for super-resolution surface nanopatterning. *Appl Phys Lett* **89**, 191125 (2006).
 37. Zhou Y, Hong MH, Fuh JYH, Lu L, Luk'yanchuk BS. Evanescent wave interference lithography for surface nano-structuring. *Phys Scr* **2007**, 35–37 (129).
 38. Sreekanth KV, Chua JK, Murukeshan VM. Interferometric lithography for nanoscale feature patterning: a comparative analysis between laser interference, evanescent wave interference, and surface plasmon interference. *Appl Opt* **49**, 6710–6717 (2010).
 39. Wang ZB, Joseph N, Li L, Luk'yanchuk BS. A review of optical near-fields in particle/tip-assisted laser nanofabrication. *Proc Inst Mech Eng, C:J Mech Eng Sci* **224**, 1113–1127 (2010).
 40. Wang WJ, Hong MH, Wu DJ, Goh YW, Lin Y et al. Ultrafast laser nanofabrication assisted with near-field scanning optical microscopy. *Proc SPIE* **5063**, 449–452 (2003).
 41. Tseng AA. Recent developments in nanofabrication using scanning near-field optical microscope lithography. *Opt Laser Technol* **39**, 514–526 (2007).
 42. Kik PG, Martin AL, Maier SA, Atwater HA. Metal nanoparticle arrays for near-field optical lithography. *Proc SPIE* **4810**, 7–13 (2002).
 43. Wang ZB, Hong MH, Luk'yanchuk BS, Huang SM, Wang QF et al. Parallel nanostructuring of GeSbTe film with particle mask. *Appl Phys A* **79**, 1603–1606 (2004).

44. Eversole D, Luk'yanchuk B, Ben-Yakar A. Plasmonic laser nanoablation of silicon by the scattering of femtosecond pulses near gold nanospheres. *Appl Phys A* **89**, 283–291 (2007).
45. Yadav RA, Singh ID. Normal modes and quality factors of spherical dielectric resonators: I — shielded dielectric sphere. *Pramana* **62**, 1255–1271 (2004).
46. Rybin MV, Koshelev KL, Sadrieva ZF, Samusev KB, Bogdanov AA et al. High-Q supercavity modes in subwavelength dielectric resonators. *Phys Rev Lett* **119**, 243901 (2017).
47. Carletti L, Koshelev K, De Angelis C, Kivshar Y. Giant nonlinear response at the nanoscale driven by bound states in the continuum. *Phys Rev Lett* **121**, 033903 (2018).

Acknowledgements

Part of the work was supported by the Tomsk Polytechnic University Development Program. This work was also supported by the Ministry of Science and Higher Education of the Russian Federation (project no. 14.W03.31.0008), in part by the Russian Science Foundation (project no. 20-12-00389), and in part by the Russian Foundation for Basic Research (projects no. 20-02-00715, no. 21-58-10005, no. 21-57-10001). Z. B.Wang acknowledges European ERDF grants (CPE 81400 and SPARCII c81133) through WEFO, and Royal society grants (IEC\NSFC\181378 and IEC\R2\202178).

Competing interests

The authors declare no competing financial interests.